Weather and climate on Mars

Conway Leovy

Department of Atmospheric Sciences, Box 351640, University of Washington, Seattle, Washington, 98195, USA
(e-mail: conway@atmos.washington.edu)

Imagine a planet very much like the Earth, with similar size, rotation rate and inclination of rotation axis, possessing an atmosphere and a solid surface, but lacking oceans and dense clouds of liquid water. We might expect such a desert planet to be dominated by large variations in day–night and winter–summer weather. Dust storms would be common. Observations and simulations of martian climate confirm these expectations and provide a wealth of detail that can help resolve problems of climate evolution.

Aside from the very limited atmospheric water and associated latent heat release, Mars' atmosphere differs from Earth's primarily in its very low surface pressure, which varies as much as 20% annually owing to seasonal CO_2 condensation at the poles[1,2] (Table 1). The corresponding low atmospheric heat capacity and short bulk radiative timescale, $<\tau_r>$, ensure that diurnal and seasonal temperature variations are much larger than those in terrestrial deserts. Maximum diurnal near-surface atmospheric temperature range is about 30 °C on Earth and about 60 °C on Mars. Seasonal daily averages of surface air temperatures range up to 90 °C in martian polar regions[1], but only up to about 50 °C in the extreme terrestrial climate of northeastern Siberia.

Martian atmospheric temperature is strongly controlled by suspended dust[3,4]. When the atmosphere is 'clear' (optical depth at visible wavelengths $\ll 1$), daytime surface heating generates convection that extends as high as 1 scale height (about 10 km, see Table 1). In this convective boundary layer, temperature decreases with height at the dry adiabatic lapse rate, about 4.3 K km^{-1}. Above this layer, temperature declines more gradually with height and can approach the limiting condensation temperature of CO_2 (130–150 K) above 40 km (refs 5, 6; Fig. 1). During the night, convection collapses and a strong temperature inversion develops in the lowest kilometre. Above 40 km, there are strong time-dependent oscillations of the vertical temperature profile, probably produced by vertically propagating waves[6]. Near winter solstice, Mars' distance from the Sun approaches its minimum, and the atmosphere becomes dusty (optical depth at visible wavelengths $\geqslant 1$). Absorption of solar radiation by dust increases the daily mean temperature and diurnal temperature range above the surface, but the surface diurnal temperature range decreases and the daytime convective layer disappears. Daily average temperature near the surface is not affected by dust loading.

Horizontal variations of temperature and associated horizontal variations of pressure drive the planetary wind system — the general circulation. Our knowledge of the general circulation of Mars is based on observations and numerical simulation models. Until very recently, these models were sophisticated but poorly constrained by data. Recent observations from the Mars Global Surveyor (MGS) now provide a good match between the degree of detail produced by the models and that available from observations. The following sections describe our present understanding of the general circulation and focus on the critical interaction between surface winds and dust storms in the present climate regime. The last section discusses the research challenge — connecting our understanding of the present climate to an improved understanding of the evolution of martian climate and surface features over the past four billion years.

The general circulation

Wind measurements are limited to surface winds at lander sites, vertical profiles of wind from the two Viking lander entry vehicles, and scattered inferences of wind from cloud features. Vertical temperature profiles inferred from thermal emission measurements, obtained primarily by Mars orbiting spacecraft, provide far more complete coverage and can be used to infer winds[7–9]. The MGS Thermal Emission Spectrometer (MGS-TES) has provided vertical temperature profiles that resolve features whose vertical scale is about 1 scale height or more[9]. In addition, Earth-based microwave measurements provide information about atmospheric temperature distribution[10]. Atmospheric

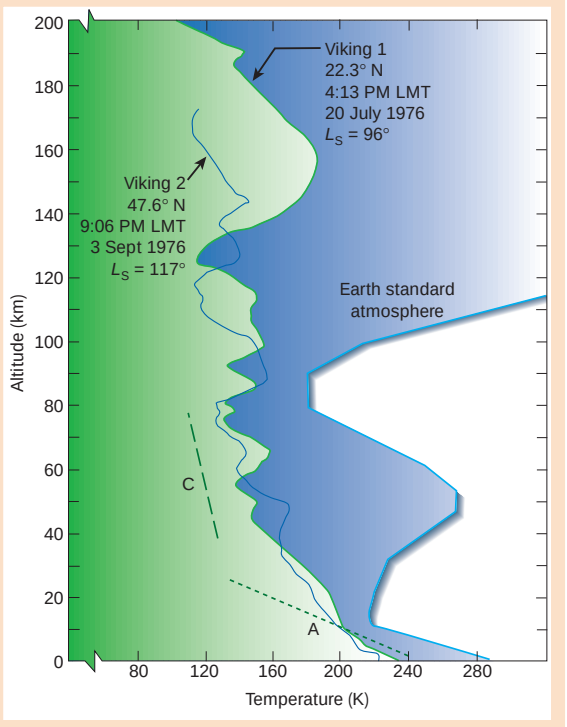

Figure 1 Mars atmosphere temperature profiles measured by Viking[5] compared with the standard atmosphere profile for Earth. Martian adiabatic lapse rate and CO_2 condensation are indicated by lines A and C, respectively. The Viking profiles are reproduced by permission of the American Geophysical Union.

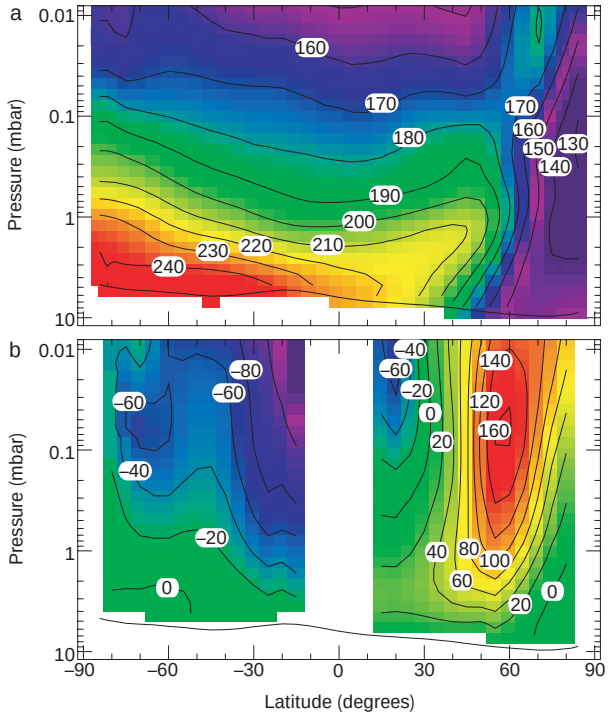

Figure 2 Cross-sections of zonal mean temperature and zonal wind for northern-hemisphere winter solstice ($L_s = 270°$) from MGS-TES observations. **a**, Temperature (K); **b**, eastward wind (m s^{-1}). Wind was derived from the thermal gradient wind approximation under the assumption that surface wind is zero everywhere (Box 1). The ordinate scale of log pressure corresponds approximately to height, with each decade roughly equivalent to 20 km, and the upper boundary near 60 km. Figure adapted from ref. 9; reproduced by permission of the American Geophysical Union.

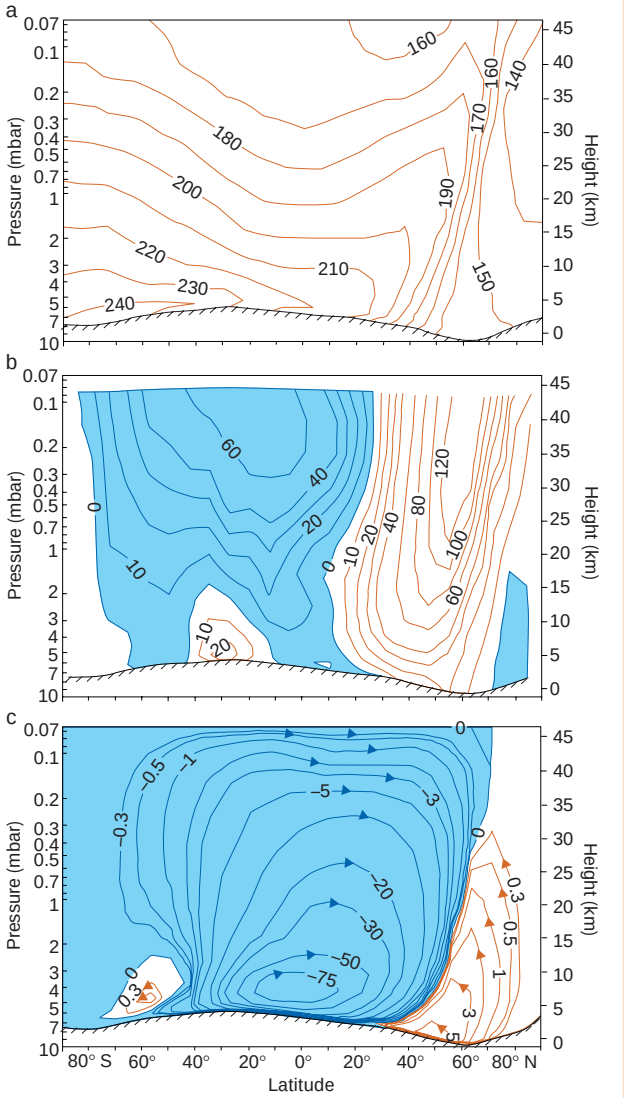

Figure 3 Zonal mean general circulation components from the GCM of Haberle *et al.*[14]. **a**, Temperature (K); **b**, west–east wind (m s^{-1}; shading corresponds to westward wind); and **c**, meridional mass stream function (10^8 kg s^{-1}; shading corresponds to clockwise circulation in the plane of the page). Simulation is for the northern winter solstice with average optical depth at visible wavelengths equal to 0.3, slightly lower than observed at this season by MGS-TES. Reproduced by permission of the American Geophysical Union.

refractive index inferred from Doppler delay of radio signals passing through the atmosphere (radio occultation) provides a limited number of temperature profiles with much higher vertical resolution[11]. These also give information about the distribution of pressure on horizontal surfaces. Time series of surface pressure are available from the sites of two Viking and one Pathfinder landed spacecraft[6,12]. Three-dimensional time-dependent distributions of temperature together with pressure on a single horizontal surface can be used to derive approximate large-scale wind fields (see Box 1). Wind distributions can also be derived through the process of assimilation of temperature data into more complete nonlinear dynamical models[13].

A representative MGS-TES temperature cross-section in the meridional plane and the corresponding zonal mean (latitude average) eastward wind field derived from thermal gradient wind balance is shown in Fig. 2. It can be compared with a meridional cross-section of temperature and total (not approximate) zonal mean eastward wind generated by a martian numerical general circulation model (GCM; Fig. 3a, b). Agreement between observed temperatures and the derived thermal gradient winds and the temperatures and winds generated by the GCM is remarkable and serves as a good test of our ability to simulate the martian general circulation[14–16]. Viking landing site and radio occultation measurements also provide some validation for the GCM surface winds[1,11]. Zonal mean mid-latitude eastward winds increase with height to maxima (jet streams) near or above the level of 3 scale heights (about 30 km) in all seasons except mid-summer, with westward wind throughout most of the subtropics and tropics. Similar zonal mean wind distributions are found on Earth, but they are weaker and the mean eastward jet streams occur at lower altitudes and latitudes. Eastward zonal winds prevail during summer at mid-latitudes on Earth, but mid-latitude zonal winds are generally westward on Mars in mid-summer. These differences in zonal winds and associated meridional temperature gradients between Mars and Earth were predicted long before spacecraft measurements became available[17]. They can be understood in terms of the thermal response to underlying oceans on Earth and underlying desert on Mars, together with the much shorter martian radiative timescale (Table 1).

The zonal mean meridional circulation, consisting of the zonally averaged poleward and upward flow components, can also be deduced approximately from the temperature field[18] (see Box 2). On Earth, this meridional circulation consists of a tropical circulation cell and a weaker mid-latitude circulation cell. The tropical cell, called the Hadley circulation, is often described in terms of an ascending branch on the Equator and descending branches near 30° in the subtropics of both hemispheres. In fact, this symmetry about the Equator is observed only near equinox. In northern winter, Earth's Hadley circulation is dominated by a single cell with ascending motion south of the Equator and descending motion in the

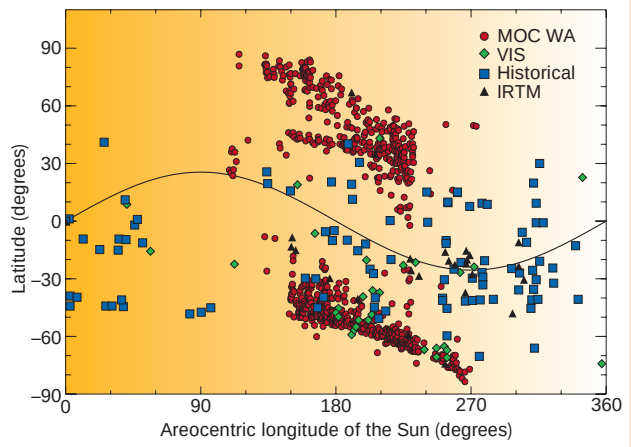

Figure 4 Local-to-regional dust storms observed by Cantor *et al.*[43]. The horizontal axis L_s is Mars-centred longitude of the Sun, an index of season. $L_s = 0°$ corresponds to northern spring equinox; $L_s = 270°$ corresponds to northern winter solstice. The figure shows all storms in the size range 10^2–1.6×10^6 km^2 observed between $L_s = 107.27$ and $L_s = 262.78$ in MGS-MOC wide angle (WA) images. Viking orbiter and historical ground-based observations of dust storms are also shown[4]. VIS and IRTM correspond respectively to storms observed by the Viking Orbiter Visible Imager and Infrared Thermal Mapper. Reproduced by permission of the American Geophysical Union.

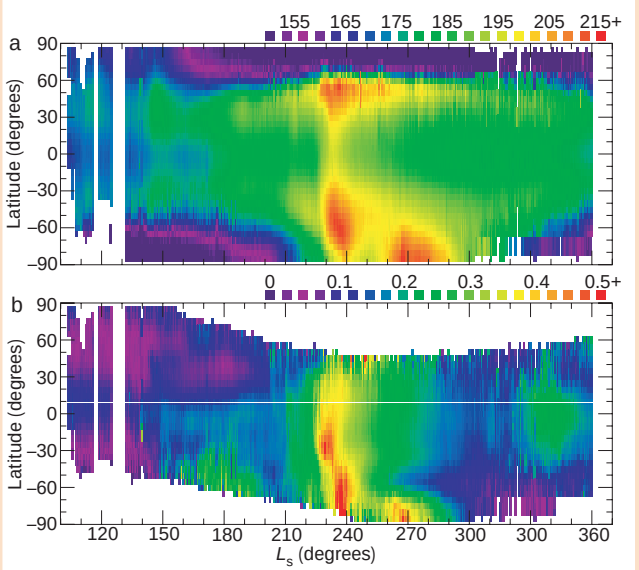

Figure 5 Temperature and dust opacity versus latitude and seasonal index (L_s) as inferred from MGS-TES by Smith *et al.*[9]. **a**, Temperature is at the 0.5-hPa level (approximately 20 km), and **b**, dust opacity at spectral wave-number 1,075 cm^{-1} is at the surface. Note the close correspondence between increased southern-hemisphere dust opacity and increased northern-hemisphere temperature, beginning near $L_s = 230$. This illustrates the global response of the Hadley circulation to enhanced heating in the southern (summer) hemisphere. Reproduced by permission of the American Geophysical Union.

northern subtropics. This pattern reverses during southern winter[19]. Similar asymmetric Hadley circulation prevails on Mars, but the circulation cells are much stronger and the ascending and descending branches are displaced much farther from the equator (30–60° latitudes)[14,20] (Fig. 3c). A symmetric, but very weak equatorially symmetric, Hadley circulation does occur on Mars, but only near the equinoxes. Because of Mars' high orbital eccentricity and resulting large seasonal differences in heating, its Hadley circulation is stronger and wider during northern winter than southern winter. Bright depositional streaks on the surface reflect the dominant Hadley circulation pattern of surface winds during this season[21,22]. In the temperature distribution of Fig. 2a, the descending branch of the Hadley circulation is evident in the temperature maximum in the latitude belt 50–60° N of the winter hemisphere.

The symmetry of the zonal mean west–east wind pattern is broken in middle latitudes by prominent large-scale wave-like flow disturbances — planetary waves. These waves are observationally well constrained from measurements at the two Viking lander sites and from MGS-TES radiance measurements. Travelling planetary waves with zonal wave numbers (number of waves around a latitude circle) from 1 to 3 occur during winter and spring in mid- and high latitudes of both hemispheres[23–25]. These propagate eastward, are well organized, and are apparently lower wave-number counterparts of eastward propagating mid-latitude weather systems on Earth. They arise from instability of the zonal mean temperature and wind fields (baroclinic and/or barotropic instability). These systems were predicted in advance of any observations[17], and they are well simulated by GCMs. Other weather systems of intermediate scale (with diameters of a few hundred kilometres) occur near the edges of the residual mid-summer north polar cap[26,27]. These systems, which produce familiar-looking moving comma-shaped cloud patterns, seem to be dry counterparts of Earth's polar lows that form primarily over open water near the sea-ice edge during winter. Stationary planetary waves (mainly zonal wave-numbers 1 and 2), generated by interaction between eastward zonal winds and the large-amplitude topography, are also observed and simulated in GCMs[28,29]. In addition, flow over topography generates internal gravity waves (or 'buoyancy waves') whose horizontal scales range from a few kilometres to several hundred kilometres (ref. 30).

The strong diurnal heating cycle generates a family of planetary waves known as thermal tides[15,31–33]; these are centred in the tropics, but extend to mid-latitudes. Evidence for thermal tides derives from large-amplitude fluctuations in vertical temperature profiles above about 40 km (Fig. 1). Most thermal tides follow the Sun westward, but interactions between Sun-following tidal components and the large-amplitude planetary topography generate additional waves. The most prominent of these are equatorially centred, eastward-propagating Kelvin waves[15,34]. Some of the energy of thermal tides and Kelvin waves propagates to elevations greater than 100 km in the upper atmosphere[35]. Absorption of upward-propagating tides and the smaller-scale internal gravity waves can strongly influence the background flow at altitudes above about 40 km (ref. 36). These waves tend to drive the background flow towards the horizontal phase speed of the waves.

Surface winds and dust storms

Surface winds calculated by GCMs are generally consistent with the few available direct measurements[37] and with the near-surface branch of the Hadley circulation inferred from MGS-TES temperature and surface dust streaks[21,22]. As on Earth, the Hadley circulation is associated with 'trade winds' blowing from the northeast in the northern hemisphere and the southeast in the southern hemisphere. These winds are confined below ±30° latitude on Earth, but extend as high as 50° latitude during the martian northern winter. During the solstice seasons, martian trade winds cross the equator, curve towards the east and form a low-elevation eastward jet in the summer subtropics[11] (Fig. 3b). This picture describes the zonal mean, but, as on Earth, the Hadley circulation winds are not longitudinally uniform. The strongest low-latitude martian surface wind probably occurs in lowlands and/or on east-facing slopes of large-scale topographic rises[38].

Strong surface wind can set particles of ~100-μm diameter into saltating motion. The resulting surface impacts can raise smaller particles into suspension to produce dust storms. Threshold wind

Box 1
Thermal wind balance

If the planetary Rossby number Ro $\ll 1$ (see Table 1), the horizontal wind vector **u** and pressure p are related by the geostrophic wind approximation: $\mathbf{u} = gH(pf)^{-1}\mathbf{k}\times\nabla_h p$, where $f = 2\Omega\sin\phi$ is the coriolis parameter at latitude ϕ, ∇_h is the gradient operator on a horizontal surface, and **k** is a 90° counterclockwise rotation operator. With the hydrostatic balance equation and the ideal gas law, this equation implies the thermal wind equation relating the vertical shear of **u** to temperature T: $\partial(\mathbf{u}/T)\partial z = g(fT^2)^{-1}\mathbf{k}\times\nabla_h T$. These approximations are usually accurate, with errors of less than 10%, for large-scale extra-tropical winds on Earth, but they must be applied with caution to Mars because Ro is larger there (Table 1). However, a slightly modified version of the thermal wind equation, the zonal thermal gradient wind equation, is very accurate outside of the deep tropics for zonal mean eastward wind u on Mars as well as Earth: $\partial(u/T)/\partial z = -g(f^*T^2)^{-1}\partial T/\partial y$, where $f^* = (f + u\tan\phi/a)$. To apply this equation, knowledge of u on some horizontal surface is required. Wind near the ground is generally much weaker than wind aloft, and surface wind can be set equal to zero as a first approximation (ref. 1, pp. 854–856).

Box 2
Zonal mean meridional circulation

In the meridional (vertical and north–south) plane, the vertical component of the flow, w, follows from an approximate version of the thermodynamic equation: $w(\Gamma_a - \Gamma) = Q/C_p = -\tau_r^{-1}(T - T_e)$, where Q is net diabatic heating rate per unit mass, T_e is local radiative equilibrium temperature, τ_r is local radiative adjustment timescale, and Γ_a and Γ are the dry adiabatic and actual lapse rates (see Table 1, and ref. 1, p. 873). Because, in the zonal average, $\Gamma_a > \Gamma$, vertical velocity is downward where $T > T_e$, and vice versa. Both T_e and τ_r depend on the dust distribution as well as on latitude, height and season, but the dust distribution can also be inferred from orbiter data[9]. The poleward wind component v can be derived from w using the zonal average continuity equation $(a\cos\phi)^{-1}\partial(v\cos\phi) = \rho^{-1}\partial(\rho w)/\partial z$.

speed for initiation of dust storms depends on surface roughness, size distribution of fine particles, and surface pressure and temperature[39]. At the two Viking lander sites, this threshold is apparently about 30 m s^{-1} for winds at 2-m height[40,41]. Although, at most sites, such strong wind speeds are rare, over an annual cycle and the planet as a whole, many local dust storms occur[42,43]. Daytime convection also generates dust devils that can extend through the depth of the convective boundary layer[44,45].

As seen in MGS Mars Orbital Camera (MGS-MOC) images, there is a strong tendency for dust storms in the size range 10^4–10^6 km^2 to occur in mid-latitude storm zones following the edge of the seasonally varying polar caps (Fig. 4). Dust storms also occur in lower latitudes, especially during northern winter when Mars is closest to the Sun. These low-latitude storms seem to be generated by a combination of the strong seasonal Hadley circulation, thermal tides, topographically forced flow and local thermal convection[46]. Dust from low-latitude storms is carried aloft by the ascending branch of the Hadley circulation and spreads widely, so that the average optical depth of the atmosphere increases from a few tenths to $\geqslant 1$ near northern winter solstice. Suspended dust strongly heats the atmosphere, inducing a powerful feedback: seasonal low-latitude winds lift dust, which leads to dust heating, which causes enhanced and enlarged Hadley circulation and thermal tides, which results in enhanced low-latitude winds. Enhancement and enlargement of the Hadley circulation is observed as dust is pumped high into the atmosphere[47–49]. This appears as an intensification and slight poleward shift of the temperature maximum in the winter-hemisphere descending branch of the Hadley circulation that coincides closely with dust-storm events in the summer hemisphere (Fig. 5). The evolution of complex dust-storm events like this one and the corresponding atmospheric dynamical response are well simulated by GCMs[15,50]. During some years, winter-solstice subtropical dust storms can expand to encircle the planet or even cover the globe[51].

Short radiative timescale and strong control of temperatures by orbital and surface properties tend to lock the martian general circulation into predictably repetitive diurnal and annual cycles, but the occasional occurrence of planet encircling and global dust storms breaks this pattern and remains poorly understood[52].

Table 1 Parameters governing the general circulations of Earth and Mars

	Earth	Mars
Mean distance from the Sun (AU)	1.0	1.52
Orbital eccentricity	0.03	0.093
Inclination of rotation axis to ecliptic	23.5°	25°
Rotation rate, Ω (10^{-4} s^{-1})	0.729	0.709
Planetary radius, a (km)	6,380	3,390
Surface gravity, g (m s^{-2})	9.81	3.72
Representative surface pressure*, p (hPa)	1,000	7 ± 1
Bulk atmospheric composition (mole fraction)	N_2(0.8), O_2(0.2), A(0.001), CO_2 (0.00037), H_2O(<0.03)	CO_2(0.95), N_2(0.03), A(0.02), H_2O (<0.0005)
Representative temperature of lowest scale height (K)	260	200
Specific gas constant, R (m^2 s^{-2} K^{-1})	287	192
Representative scale height, RT/g (km)	7.6	10.3
Specific heat at constant pressure, C_p (m^2 s^{-2} K^{-1})	1,000	860
Dry adiabatic lapse rate, Γ_a ($=-g/C_p$) (K km^{-1})	9.8	4.3
Average lapse rate of lowest scale height, Γ (K km^{-1})	6.5	2.5
Bulk radiative timescale, $<\tau_r>$ (10^5 s)	40	2
Typical zonal wind at jet level, U (m s^{-1})	30	80
Planetary Rossby number, Ro ($=U/\Omega a$)	0.05	0.2

*Mars surface-pressure data correspond to approximate global mean annual average and annual range, not uncertainty.

The research challenge

Lifting and transport of dust produce non-uniform surface erosion and deposition[53] and have substantially modified the surface of Mars over the past four billion years. If periods of higher surface pressure occurred in the past, threshold wind speeds for saltation would have been lower, and wind would have been a much more effective agent of surface modification. Variations in orbital parameters should also have produced substantial changes in the magnitude and distribution of net dust transport. Variations in tilt of the rotation axis (obliquity), whose range is approximately 15–40° in the present epoch, eccentricity, and argument of perihelion will generate large changes in the intensity and size of the Hadley circulation and in planetary waves. Because these meteorological factors interact with the large-amplitude martian topography, which is highly asymmetric about the equator, substantial transport between low- and high-elevation regions as well as substantial meridional transport should have occurred over the past four billion years. These factors complicate the geological interpretation of surface features. One of the main challenges is to integrate martian GCM simulations of past climates with studies of surface geology to decipher the record of martian climate history and the roles of impacts, volcanism, wind, ice and water in modifying the surface over time (see review in this issue by Jakosky and Phillips, pages 237–244). The good agreement between observations, theory and models of the present martian climate provides a solid basis for addressing this challenge. □

1. Zurek, R. et al. in Mars (eds Kieffer, H. H., Jakosky, B. M., Snyder, C. W. & Matthews, M. S.) 835–933 (Univ. Arizona Press, Tucson, 1992).
2. James, P., Kieffer, H. & Paige, D. in *Mars* (eds Kieffer, H. H., Jakosky, B. M., Snyder, C. W. & Matthews, M. S.) 934–968 (Univ. Arizona Press, Tucson, 1992).
3. Gierasch, P. & Goody, R. The effect of dust on the temperature of the Mars atmosphere. *J. Atmos. Sci.* **29,** 400–402 (1972).
4. Kahn, R., Martin, T., Zurek, R. & Lee, S. in *Mars* (eds Kieffer, H. H., Jakosky, B. M., Snyder, C. W. & Matthews, M. S.) 1017–1053 (Univ. Arizona Press, Tucson, 1992).
5. Seiff, A. & Kirk, D. Structure of the atmosphere of Mars in summer at mid-latitudes. *J. Geophys. Res.* **82,** 4364–4378 (1977).
6. Schofield, J. *et al.* The Mars Pathfinder Atmospheric Structure Investigation/Meterology (ASI/MET) experiment. *Science* **278,** 1752–1758 (1997).
7. Martin, T. & Kieffer, H. Thermal infrared measurements of the martian atmosphere 2. The 15 μm band measurements. *J. Geophys. Res.* **84,** 2843–2852 (1979).
8. Wilson, R. & Richardson, M. The martian atmosphere during the Viking mission: infrared measurements of atmospheric temperatures revisited. *Icarus* **145,** 555–579 (2000).
9. Smith, M. *et al.* TES observations of atmospheric thermal structure and aerosol distribution during MGS mapping. *J. Geophys. Res.* **106** (in the press).
10. Clancy, R. *et al.* An intercomparison of ground-based millimeter, MGS TES, and Viking atmospheric temperature measurements: seasonal and interannual variability of temperatures and dust loading in the global Mars atmosphere. *J. Geophys. Res.* **105,** 9553–9571 (2000).
11. Hinson, D. *et al.* Initial results from radio occultation measurements with Mars Global Surveyor. *J. Geophys. Res.* **104,** 26997–27012 (1999).
12. Tillman, J., Johnson, N., Guttorp, P. & Percival, D. The martian annual pressure cycle: years without great dust storms. *J. Geophys. Res.* **98,** 10963–10971 (1993).
13. Lewis, S. *et al.* A climate database for Mars. *J. Geophys. Res.* **104,** 24177–24194 (1999).
14. Haberle, R. *et al.* Mars atmospheric dynamics as simulated by the NASA/Ames general circulation model, 1. The zonal-mean circulation. *J. Geophys. Res.* **102,** 13301–13311 (1993).
15. Wilson, J. & Hamilton, K. Comprehensive model simulation of thermal tides in the martian atmosphere. *J. Atmos. Sci.* **53,** 1290–1326 (1996).
16. Forget, F. *et al.* Improved general circulation models of the Martian atmosphere from the surface to above 80 km. *J. Geophys. Res.* **104,** 24156–24175 (1999).
17. Mintz, Y. in *The Atmospheres of Mars and Venus* (eds Kellogg, W. & Sagan, C.) NAS-NRC Publication 944, 107–146 (National Research Council, Washington DC, 1961).
18. Santee, M. & Crisp, D. Thermal structure and dust loading of the martian atmosphere during late summer: Mariner 9 revisited. *J. Geophys. Res.* **98,** 3261–3279 (1993).
19. Hartmann, D. *Global Physical Climatology* 140–143 (Academic, San Diego, 1994).
20. Conrath, B. *et al.* Mars Global Surveyor Thermal Emission Spectrometer (TES) observations: atmospheric temperatures during aerobraking and science phasing. *J. Geophys. Res.* **104,** 9509–9519 (1999).
21. Thomas, P., Veverka, J., Gineris, D. & Wong, L. "Dust" streaks on Mars. *Icarus* **49,** 398–415 (1984).
22. Greeley, R., Skypeck, A. & Pollack, J. Martian aeolian features and deposits: comparisons with general circulation model results. *J. Geophys. Res.* **98,** 3183–3196 (1993).
23. Barnes, J. Midlatitude disturbances in the Martian atmosphere: a second Mars year. *J. Atmos. Sci.* **38,** 225–234 (1981).
24. Barnes, J. Linear baroclinic instability in the Martian atmosphere. *J. Atmos. Sci.* **41,** 1536–1550 (1984).
25. Hollingsworth, J. *et al.* Orographic control of storm zones on Mars. *Nature* **380,** 413–416 (1996).
26. Gierasch, P., Thomas, P., French, R. & Veverka, J. Spiral clouds on Mars: a new atmospheric phenomenon. *Geophys. Res. Lett.* **6,** 405–408 (1979).
27. James, P., Hollingsworth, J., Wolff, J. & Lee, S. North polar dust storms in early spring on Mars. *Icarus* **38,** 64–73 (1999).
28. Conrath, B. Planetary-wave structure in the Martian atmosphere. *Icarus* **48,** 246–255 (1981).
29. Hollingsworth, J. & Barnes, J. Forced stationary planetary waves in Mars's winter atmosphere. *J. Atmos. Sci.* **53,** 428–448 (1996).
30. Briggs, G. & Leovy, C. Mariner 9 observations of the Mars north polar hood. *Bull. Am. Meteorol. Soc.* **55,** 278–296 (1972).
31. Zurek, R. Diurnal tide in the martian atmosphere. *J. Atmos. Sci.* **33,** 321–337 (1976).
32. Zurek, R. & Leovy, C. Thermal tides in the dusty Martian atmosphere: a verification of theory. *Science* **213,** 437–439 (1981).
33. Hinson, D., Hollingsworth, J., Wilson, R. & Tyler, G. Radio occultation measurements of forced atmospheric waves on Mars. *J. Geophys. Res.* **106** (in the press).
34. Tillman, J. Mars global atmospheric oscillations: annually synchronized, transient normal mode oscillations and the triggering of global dust storms. *J. Geophys. Res.* **93,** 9433–9451 (1988).
35. Keating, G. *et al.* Evidence for large global diurnal Kelvin wave in the Mars upper atmosphere. *Bull. Am. Astron. Soc.* **32,** Abstr. 50:02 (2000).
36. Zurek, R. & Haberle, R. Zonally symmetric response to atmospheric tidal forcing in the dusty Martian atmosphere. *J. Atmos. Sci.* **45,** 2469–2485 (1988).
37. Murphy, J., Leovy, C. & Tillman, J. Observations of martian surface winds at the Viking Lander 1 site. *J. Geophys. Res.* **95,** 14555–14576 (1990).
38. Joshi, M., Lewis, S., Read, P. & Catling, D. Western boundary currents in the atmosphere of Mars. *Nature* **367,** 548–551 (1994).
39. Greeley, R., Lancaster, N., Lee, S. & Thomas, P. in *Mars* (eds Kieffer, H. H., Jakosky, B. M., Snyder, C. W. & Matthews, M. S.) 835–933 (Univ. Arizona Press, Tucson, 1992).
40. Ryan, J., Sharman, R. & Lucich, R. Local Mars dust storm generation mechanism. *Geophys. Res. Lett.* **8,** 899–901 (1981).
41. Arvidson, R. *et al.* Three Mars years: Viking lander imaging observations. *Science* **222,** 463–468 (1983).
42. Peterfreund, A. & Kieffer, H. Thermal and infrared properties of the martian atmosphere. 3: Local dust clouds. *J. Geophys. Res.* **84,** 2853–2862 (1979).
43. Cantor, B., James, P., Caplinger, M. & Wolff, M. Martian dust storms: 1999 Mars Orbiter Camera observations. *J. Geophys. Res.* **106** (in the press).
44. Ryan, J. & Carroll, J. Dust devil wind velocities: mature state. *J. Geophys. Res.* **75,** 531–541 (1970).
45. Thomas, P. & Gierasch, P. Dust devils on Mars. *Science* **230,** 175–177 (1985).
46. Leovy, C., Zurek, R. & Pollack, J. Mechanisms of Mars dust storms. *J. Atmos. Sci.* **30,** 749–762 (1973).
47. Leovy, C., Tillman, J., Guest, W. & Barnes, J. in *Recent Advances in Planetary Meteorology* (ed G. Hunt) 69–84 (Cambridge Univ. Press, Cambridge, 1985).
48. Anderson, E. & Leovy, C. Mariner 9 television limb observations of dust and ice hazes on Mars. *J. Atmos. Sci.* **35,** 723–234 (1978).
49. Smith, M., Pearl, J., Conrath, B. & Christensen, P. Mars Global Surveyor Thermal Emission Spectrometer (TES) observations of dust opacity during aerobraking and science phasing. *J. Geophys. Res.* **105,** 9539–9552 (2000).
50. Murphy, J. *et al.* Three-dimensional numerical simulation of Martian global dust storms. *J. Geophys. Res.* **100,** 26357–26376 (1995).
51. Zurek, R. & Martin, L. Interannual variability of planet-encircling dust storms on Mars. *J. Geophys. Res.* **98,** 3247–3259 (1993).
52. Haberle, R. Interannual variability of global dust storms on Mars. *Science* **234,** 459–461 (1986).
53. Anderson, F. *et al.* Assessing the Martian surface distribution of aeolian sand using a Mars general circulation model. *J. Geophys. Res.* **104,** 18991–19002 (1999).

Acknowledgements

I thank M. Smith for making available Figs 2 and 5, and B. Cantor for making available Fig. 4.